*Radio Science*, Volume 32, Number 5, Pages 1821–1832, September–October 1997

# Calibration and experimental results of a two-dimensional interferometric radiometer laboratory prototype

A. Camps, F. Torres, I. Corbella, J. Bará,and X. Soler

Department of Signal Theory and Communications, Universitat Politècnica de Catalunya, Barcelona, Spain

**Abstract.** In recent years, Earth observation by means of aperture synthesis radiometry has received special attention by some space agencies as a possible solution to achieve high radiometric accuracy and spatial resolution at low microwave frequencies (L band), where the apparent brightness temperature is much more sensitive to soil moisture and sea surface salinity. This paper presents the characterization and calibration procedure, as well as some synthetic images measured with an X band experimental Y-shaped Synthetic Aperture Interferometric Radiometer prototype developed at the Polytechnic University of Catalonia. The instrument is composed of a single pair of antennas that can be moved along the arms of an Y structure to synthesize a set of baselines. An experimental procedure is proposed to evaluate and then calibrate offset, inphase, quadrature, and amplitude errors generated by receivers and correlators.

## 1. Introduction

As stated in the Soil Moisture and Ocean Salinity consultative meeting (SMOS) held at the European Space Agency (ESA)/European Space Research and Technology Centre (ESTEC) during April 20-21, 1995, Synthetic Aperture Interferometric Radiometers (SAIRs) need to develop "calibration methods and data processing algorithms" (recommendation number 3). The object of the Synthetic Aperture Interferometric Radiometer (SAIR) demonstrator is the characterization of instrument subsystems, the characterization of its performance, its calibration and the synthesis of some apparent brightness temperature images.

While a total power radiometer measures the power collected in the main beam direction, interferometric radiometers measure the complex correlation between the signals collected by a pair of spaced antennas. This basic measurement, also called visibility sample $V_{12}(u,v)$, is related to the brightness temperature distribution by [*Thompson et al.*, 1986]

$$V_{12}(u,v) = \frac{1}{2} E\left[S_{a_1}(t) S_{a_2}^*(t)\right] \tag{1}$$



Paper number 97RS01268.
0048-6604/97/97RS-01268$11.00

$$= \iint_{\xi^2+\eta^2\le 1} T(\xi,\eta)\, \tilde{r}_{12}\left(-\frac{u\xi+v\eta}{f_o}\right) e^{-j\,2\pi\,(u\xi+v\eta)}\, d\xi\, d\eta$$

$$T(\xi,\eta) = \frac{T_B(\xi,\eta)}{\sqrt{1-\xi^2-\eta^2}}\, F_{n_1}(\xi,\eta)\, F_{n_2}^*(\xi,\eta) \tag{2}$$

where

$S_{am}(t)$ analytic signals of the voltages collected by antennas $m = 1, 2$, equal to $i_m(t) + j\, q_m(t)$;

$(u,v)$ spacing between the two antennas in wavelengths, equal to $(X_2\text{-}X_1, Y_2\text{-}Y_1)/\lambda$;

$(\xi,\eta)$ direction cosines with respect to $(X, Y)$ axes (Figure 1), equal to $(\sin\theta\cos\phi,\ \sin\theta\sin\phi)$;

$T_B(\xi,\eta)$ brightness temperature (kelvins);

$T(\xi,\eta)$ so-called modified brightness temperature (kelvins);,

$1/\sqrt{1-\xi^2-\eta^2}$ obliquity factor;

$F_{nm}(\xi,\eta)$ normalized antenna voltage pattern of antenna $m$;

$\tilde{r}_{12}(t)$ so-called fringe-wash function that takes into account spatial decorrelation effects and depends on receivers' responses through

$$\tilde{r}_{12}(t) = r_{12}(t)\, e^{-j2\pi f_o t}$$

$$r_{12}(t) = \int_0^\infty H_{n_1}(f)\, H_{n_2}^*(f)\, e^{j2\pi f t}\, df \tag{3}$$

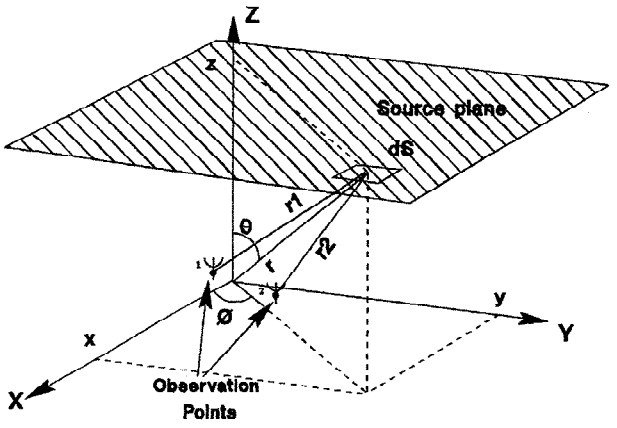


**Figure 1.** Antenna and thermal source geometry.

and where $H_{nm}(f)$ is the normalized band-pass voltage transfer function of receiver $m$ ($|H_{nm}(f)|_{max}=1$) and $f_o$ is the central frequency.

Note that when decorrelation effects are negligible ($\tilde{r}(t) \approx 1$) and all the antennas have the same voltage radiation pattern equation (1) becomes a Fourier transform between the visibility function and the modified brightness temperature $T(\xi,\eta)$:

$$T(\xi,\eta) = F^{-1}[V(u,v)] \quad (4)$$

## 2. Instrument Description

It is clear from equation (1) that a basic receiver must amplify and then correlate the thermal noise collected by a pair of antennas. Following the technique described by *Laursen and Skoſu* [1994] and *Peichl and Süβ* [1994], the instrument is formed only by a single baseline consisting of two antennas, two receiver chains, and a complex 1 bit/2 level digital correlator (1B/2L). The complete set of baselines of a static scene is then measured by moving the antennas along an Y array and measuring the correlation at each position. The main characteristics of the instrument are input frequency 10.7 GHz, equivalent noise bandwidth 30 MHz, equivalent noise temperature $T_{R1}$= 120 K, $T_{R2}$= 90 K, and adjustable gain between 93 and 107 dB. The choice of the center frequency, 10.7 GHz instead of 1.4 GHz, is based on the availability of commercial elements and the reduction of the size of the structure, while remaining in a protected band. As shown in Figures 2 and 3,

1. The interferometer is composed for a polyvinyl chloride (PVC) Y-shaped structure mounted over a tripod where two 10.7 GHz cup-dipole antennas are placed. Cup-dipole antennas have been selected because of their small size: 0.89 λ diameter, their wide antenna pattern: about 70° half-power beam

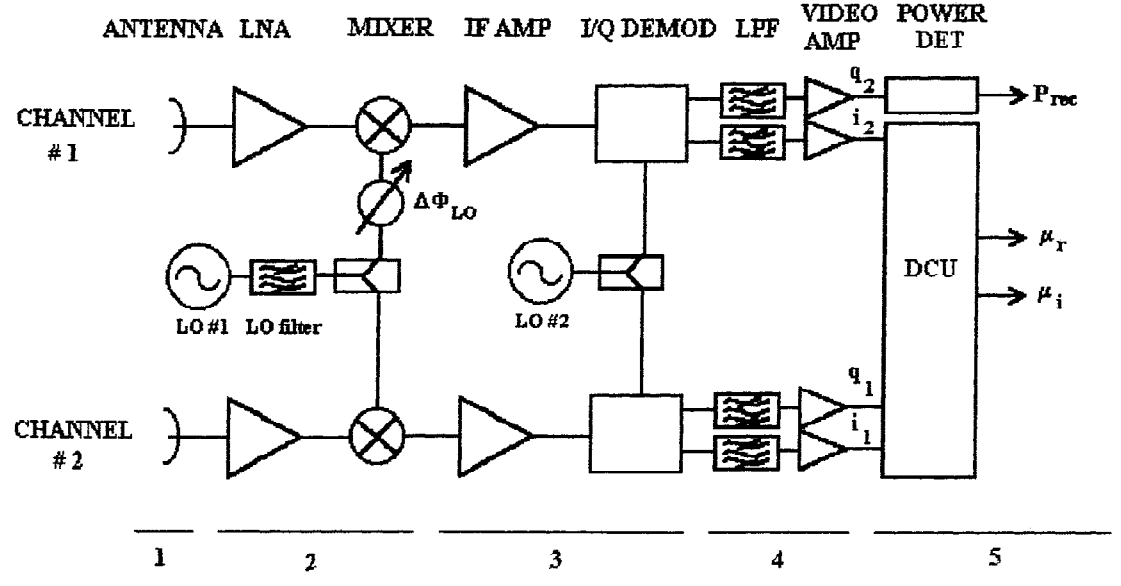


**Figure 2.** Experimental interferometric radiometer scheme: 1, antennas; 2, RF front end; 3, IF section; 4, LF section; 5, 66 MHz 1bit/2 level digital correlators and power detector.

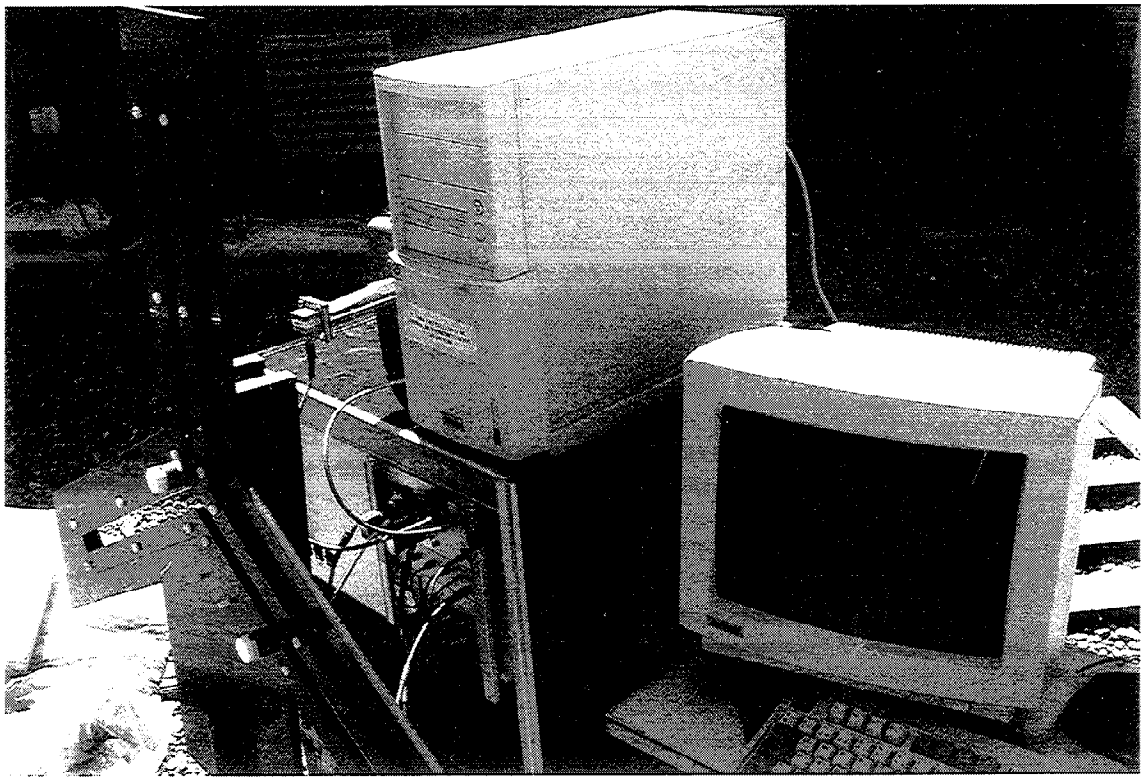

**Figure 3.** Experimental interferometric radiometer picture: 1, PVC Y structure; 2, two cup-dipole antennas; 3, mainframe

width, and their low coupling: less than 30 dB at 0.89 λ.

2. The RF front end is formed by two X band down converters that allow coherent down conversion from 10.7 GHz to 881.5 MHz. Its main characteristics are 45 dB gain, and 1.2-1.5 dB noise figures. Filtering is performed at the IF stage in order to prevent noise figure degradation. As will be shown in section 3, a phase shifter is inserted in one branch of the local oscillator for phase calibration purposes.

3. The IF section amplifies and then demodulates the inphase and quadrature components in order to perform the correlation at baseband by means of real correlators. IF gain is 25 dB, and IF bandwidth is set to 40 MHz to reject possible interferant signals.

4. The LF section is formed by a bank of four 7th order, 21.4 MHz half-power bandwidth Chebyschew filters that determine system's bandwidth. An adjustable gain video amplifier (23-37 dB) is required to drive the comparators of the 1B/2L Digital Correlator Unit (DCU) that sample the input signals at a 66 MHz rate. The DCU computes the real and imaginary parts of the visibility samples from the correlation of the inphase signals $i_1$-$i_2$ and the mixed correlation of a quadrature signal with and inphase one $q_1$-$i_2$, using the following expression

$$V_{12}(u,v) = \frac{1}{2}E\left[S_{a_1}(t)\,S_{a_2}{}^*(t)\right] \equiv R_{i_1 i_2}(0) + j\,R_{q_1 i_2}(0) \tag{5}$$

5. The 1B/2L DCU uses high speed comparators that implement the "sign" function and Fast-Transistor Transistor Logic (TTL) technology. The DCU is controlled by a signal acquisition board and a C++ program. This program controls the integration time: adjustable from 1 ms to 64 s, the calibration routines: offset, inphase, quadrature, and amplitude, and establishes the sequence of antenna positions during the measurement.

The 1B/2L DCU computes the correlation as the ratio of the counts in which there is coincidence in the sign of the two signals being correlated (sign($x$) = sign($y$)) to the total number of counts ($N_{\text{total}}$).

$$Z_{xy}(0) = \frac{N_{\text{sign}(x)=\text{sign}(y)}}{N_{\text{total}}}; \quad 0 \le Z_{xy}(0) \le 1 \tag{6}$$

$$\rho_{xy} = 2(Z_{xy} - 1); \quad -1 \le \rho_{xy} \le 1$$

where $x=i_1$ or $q_1$ and $y=i_2$ (equation (5)). The normalized correlation can be easily derived from [*Hagen and Farley*, 1973]

$$\mu_{xy} = \sin\left(\frac{\pi}{2}\rho_{xy}\right) \tag{7}$$

and the amplitude information lost in the comparator is recovered through

$$V_{12_r} = R_{i_1 i_2}(0) = \sqrt{(T_A + T_{R_1})(T_A + T_{R_2})}\ \mu_{i_1 i_2}$$
$$V_{12_i} = R_{q_1 i_2}(0) = \sqrt{(T_A + T_{R_1})(T_A + T_{R_2})}\ \mu_{q_1 i_2} \tag{8}$$

where $T_A+T_{R1}$ and $T_A+T_{R2}$ are the average noise temperatures of the signals being correlated. At this point it must be pointed out that due to the low antenna pattern mismatches and the low antenna coupling, the antenna patterns do not vary significantly for different antennna positions and the antenna temperature can be assumed to be the same for both antennas. It is also assumed that $T_A$ does not vary significantly during the measurement sequence. This parameter is estimated with the total power radiometer that measures the power of signal $q_2(t)$ (Figure 2).

## 3. Instrument Characterization and Calibration

System errors that are taken into account are modeled as follows, in order to be measured and calibrated:

$$\begin{bmatrix}\mu_r^{(4)}\\ \mu_i^{(4)}\end{bmatrix} = \begin{bmatrix}\cos(\Delta\phi) & \sin(\Delta\phi)\\ -\sin(\Delta\phi) & \cos(\Delta\phi)\end{bmatrix}\begin{bmatrix}1 & 0\\ -\sin(\theta_q) & \cos(\theta_q)\end{bmatrix}$$
$$\begin{bmatrix}gg_r & 0\\ 0 & gg_i\end{bmatrix}\begin{bmatrix}\mu_r^{(1)}\\ \mu_i^{(1)}\end{bmatrix} + \begin{bmatrix}\mu_{r_{\text{offset}}}\\ \mu_{i_{\text{offset}}}\end{bmatrix} \tag{9}$$

$$\overline{\mu^{(4)}} = \overline{\overline{P_{\Delta\phi}}}\ \overline{\overline{P_{\theta_q}}}\ \overline{\overline{g}}\ \overline{\mu^{(1)}} + \overline{\mu_{\text{offset}}}$$

where

$$\Delta\phi = \phi_{0_1} - \phi_{0_2} + \Delta\phi_{\text{OL}} \tag{10}$$

$\Delta\phi_{\text{OL}}$ is the phase shift introduced in the oscillator of one chain to calibrate inphase errors (Figure 2), $gg_r$ and $gg_i$ are the absolute gain loss factors due to differences in the receiver's frequency response in the channels $i_1$-$i_2$ and $q_1$-$i_2$ respectively, and $\mu_{r\ \text{offset}}$ and $\mu_{i\ \text{offset}}$ are their offsets.

### 3.1. Calibration of offset errors

Offset errors are originated from 1B/2L comparators' threshold errors and oscillator's thermal noise present over the RF band that leaks to the IF through the mixers. Offset errors are measured by placing a matched load in front of each receiver. Note that in this case (equation (9)), $\mu_r^{(1)}$ and $\mu_i^{(1)}$ are zero and the offset term is measured. Once the offset terms are known, they are removed from each measurement as

$$\begin{bmatrix}\mu_r^{(3)}\\ \mu_i^{(3)}\end{bmatrix} = \begin{bmatrix}\mu_r^{(4)}\\ \mu_i^{(4)}\end{bmatrix} - \begin{bmatrix}\mu_{r_{offset}}\\ \mu_{i_{offset}}\end{bmatrix} \tag{11}$$

Note that $\mu_{r,i}^{(3)}$ contains inphase and quadrature phase errors, as well as amplitude errors. In order to have a good radiometric accuracy, offset calibration is performed during a long period of time, usually of the order of 20-30 s, for which the radiometric sensitivity is about $\sigma_{\mu r,i} = 2\ 10^{-5}$ or, equivalently, $\sigma_{V_{r,i}} = 0.008$ K. Measured offset drifts are small, even for long measurement periods, with peak-to-peak drifts as small as $\Delta V_{r,i} = 0.18$ K during 90 min.

### 3.2. Calibration of amplitude and quadrature errors

Since 1B/2L digital correlators compute the normalized correlation from the sign of the signals being correlated, receiver's gain fluctuations do not introduce amplitude errors. Amplitude and quadrature errors are due to mismatches in the channel's frequency response and errors in the sampling times in the comparators of the real and imaginary channels of the 1B/2L DCU. In this section a new procedure is devised to characterize, measure, and then calibrate overall system's amplitude and quadrature errors, neglecting their origin: I/Q demodulators, receivers' frequency response, correlators, etc. This technique consists of measuring the so-called "calibration circles": the response of both real and imaginary channels to correlated noise, when the phase of the local oscillator of one receiver varied (Figure 2). In order to avoid receiver saturation when injecting correlated noise, it is convenient to have the same input power as when measuring the noise collected by

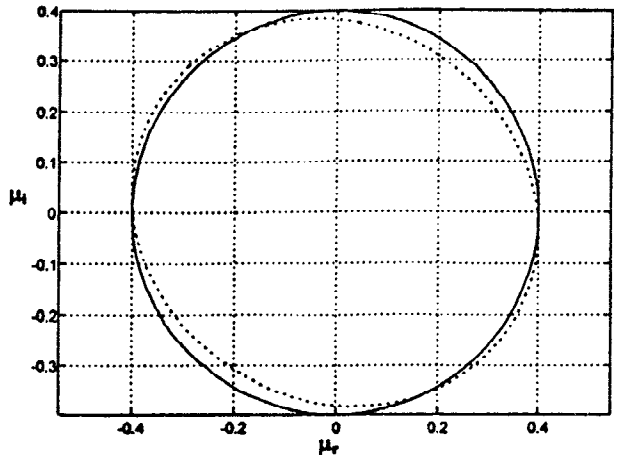


**Figure 4.** "Calibration circles": graphical calibration of overall amplitude and quadrature errors (dotted circle, uncalibrated; solid circle, calibrated).

the antennae; that is, $T_{noise} \approx T_A$. It presents a major problem, since any passive power splitter with isolated outputs (i.e, a Wilkinson power divider) contains at least one resistor that also introduces correlated noise. In addition, the noise generated in the Wilkinson's resistance is in 0°-180° phase at its outputs and gives a correlation opposite of that given by the matched load at the same physical temperature connected at the Wilkinson's input. Therefore noise must be injected through a nonresistive power splitter. However, since its outputs are not isolated, front end inputs must be well matched to avoid interaction between noise injected in the two receivers. In this situation the theoretical real and imaginary correlations should vary according to (Figure 4, dotted line)

$$\mu_r^{(3)\,ideal} = \mu_r^{(2)} = \mu_0 \cos(\Delta\phi)$$

$$\mu_i^{(3)\,ideal} = \mu_i^{(2)} = \mu_0 \sin(\Delta\phi) \qquad (12)$$

$$\mu_0 = \frac{T_{ph}/2}{\sqrt{\left(T_{ph}/2 + T_{R_1}\right)\left(T_{ph}/2 + T_{R_2}\right)}}$$

where $\mu_0$ is the modulus of the correlation and $T_{ph}$ is the physical temperature of the matched load connected to the nonresistive power splitter. However, when amplitude and I/Q errors are present, the measured normalized correlations take the form ($\mu_r^{(3)}$, $\mu_i^{(3)}$) (Figure 4, solid line) [*Torres et al.*, 1996]

$$\mu_r^{(3)} \equiv g g_r \mu_r^{(2)};\ g_r \triangleq 1$$

$$\mu_i^{(3)} = g g_i \mu_i^{(2)} \cos(\theta_q) - g g_r \mu_r^{(2)} \sin(\theta_q) \Rightarrow (13)$$

$$\Rightarrow \quad \mu_i^{(2)} = \frac{\frac{1}{g}\mu_i^{(3)} + \mu_r^{(2)} \sin(\theta_q)}{g_i \cos(\theta_q)}$$

from which the calibrated correlations can be extracted. The unknowns $\theta_q$ and $g_i$ are found by adjusting the set of measurements to a circle by the least squares method. Prior to the optimization process the value of gain $g$ must be determined (see section 3.4). Overall relative amplitude error in the imaginary channel is found to be $g_i = 0.96$. Overall quadrature error is found to be about $\theta_q = -5.55°$. Figure 5 shows the quadrature error measured for both I/Q demodulators. Note that this error is not constant throughout the band. Calibration gives an average value of these quadrature errors [*Torres et al.*, 1996]. Moreover, the proposed procedure takes also into account quadrature errors introduced by misalignment of the comparators' sampling times [*Camps et al.*, 1997a]. The ratio between the axes of the ellipse shown in Figure 4 decreases from 1.13 down to 1.02.

A major advantage of this method is that amplitude and quadrature errors are calibrated independently of inphase errors $\phi_{01}$ - $\phi_{02}$ (equation (10)).

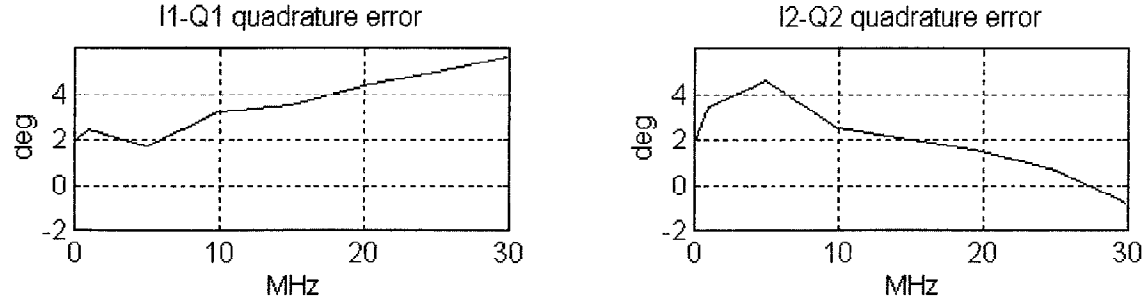


**Figure 5.** Measured I/Q demodulators quadrature error (Minicircuits MIQC-895 D)

### 3.3. Hardware calibration of inphase errors

Hardware calibration of the inphase errors is performed by adjusting the phase of the LO at one of the receivers when injecting correlated noise (Figure 2). This procedure is performed by correlating correlated noise as in section 3.2 during integration times of the order of 3 s. At each step the phase shifter is adjusted until the imaginary part of the normalized correlation being measured is zero. Note that this forces in equation (9) that

$$\overline{\mu^{(2)}} = \overline{\mu^{(1)}};$$
$$\overline{\overline{P_{\Delta\phi}}} \triangleq \begin{bmatrix} 1 & 0 \\ 0 & 1 \end{bmatrix}; \quad \phi_{0_1} - \phi_{0_2} + \Delta\phi_{LO} = 0 \tag{14}$$

### 3.4. Determination of the overall gain loss factor $g$ by measuring the fringe-wash function

The fringe-wash function (equation (3)) is the self-correlation function of the filtered noise. It measures the decorrelation suffered from a signal when it is correlated with a delayed version of itself. The fringe-wash response of the interferometer is measured by injecting correlated noise to both channels with the nonresistive power splitter with different delays that are generated by inserting several coaxial cables in the path of the $i_1$ baseband signal. This introduces a delay while the channel's phase remains nearly constant. Time delay for each coaxial is measured by means of a reflectometer.

To minimize the uncertainty of the measured receivers noise temperature and to improve the accuracy, noise is generated with a Hewlett-Packard wideband noise source with an excess noise ratio of ENR=15 dB, which is equivalent to a matched load at a physical temperature of

$$T_{source} = \frac{1}{2} 290 \left(10^{ENR/10} - 1\right) \approx 4.440 \text{ K} \tag{15}$$

The theoretical modulus of the normalized correlation at $\tau = 0$ is then given by

$$\mu_0 = \frac{T_{source}}{\sqrt{T_{source} + T_{R_1}}\sqrt{T_{source} + T_{R_2}}} \approx 0.977 \tag{16}$$

which is very close to unity.

Figure 6 shows the measured correlation for different time delays. As it is appreciated in Figure 6 for small time delays ($\tau < 10$ ns), the fringe-wash function is best fitted by a Gaussian function (filters modeled by a Gaussian function), while for large delays the secondary lobes are best fitted by a "sinc" function (filters modeled by a rectangle). The correlation measured at the origin is 0.827, due to differences in the receivers' frequency response. Since the normalized correlation should be $\mu_0 = 0.977$, the overall gain factor is $g$=0.827/0.977 = 0.846.

### 3.5. Radiometric sensitivity characterization

Radiometric sensitivity is defined as the minimum detectable change in the recovered apparent brightness temperature map, and it is related to the noise in each baseline measured [*Thompson et al.*, 1986]; [*Bará et al.*, 1996]; [*Camps*, 1996]

$$\Delta T \approx \frac{\sqrt{3}}{2} d^2 \sqrt{\sum_m \sum_n W_{mn}^2}\, \sigma_{V_{mn}} \tag{17}$$

where $d$ is the spacing between adjacent antenna

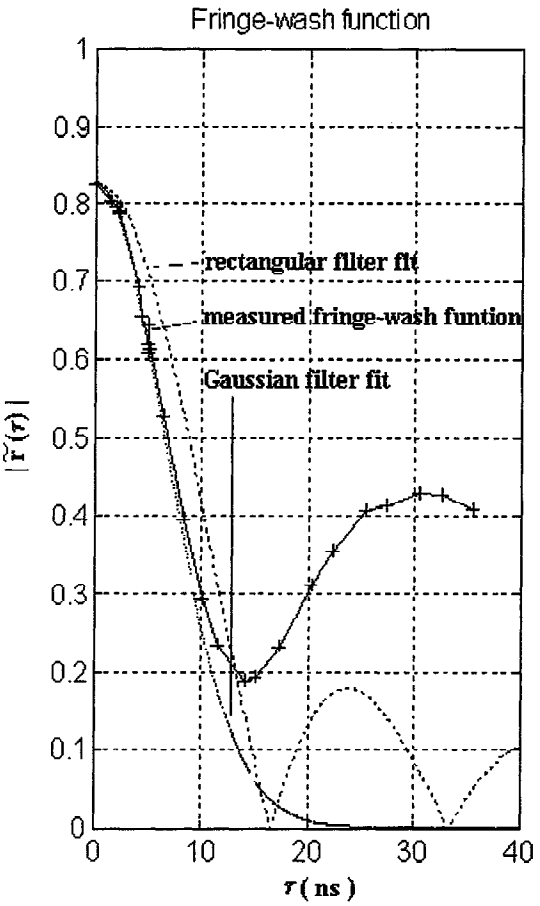


**Figure 6.** Measured fringe-wash function (plusses), Gaussian fit (solid line), and rectangular fit (dotted line).

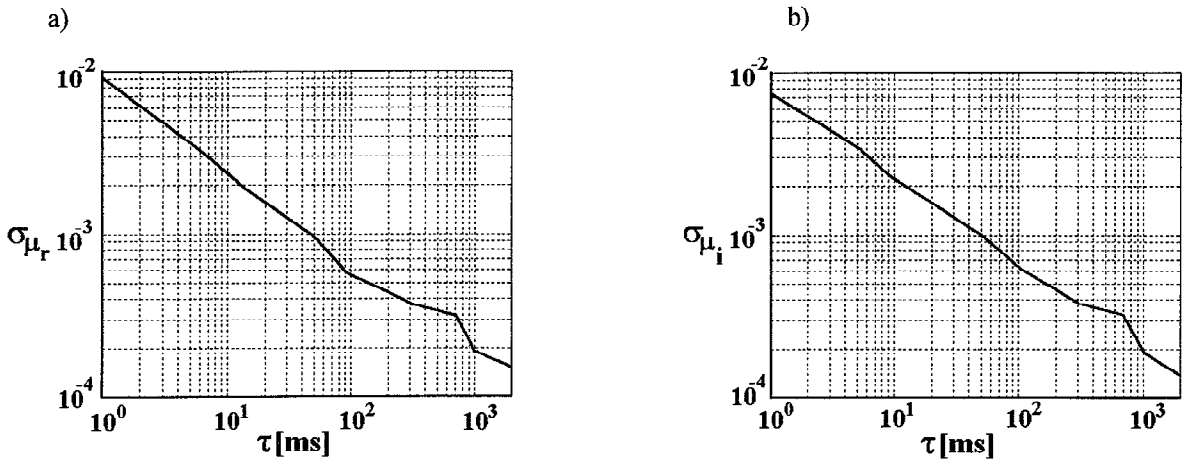


**Figure 7.** Radiometric sensitivity of the (a) real and (b) imaginary parts of the normalized visibility.

positions along the Y arms: $d = 0.89$ wavelengths, and $W_{mn}$ is the window used to weight the visibility sample $V(u_{mn}, v_{mn})$.

The radiometric sensitivity can be then characterized by connecting two different matched loads to the front ends' inputs. The standard deviation in the visibility samples $\sigma_{V_{r,i}}$ is then computed from a large set of measurements for different integration times. When two different matched loads are connected to the inputs of the front end, the correlator's output must be zero except for small offset errors that have already been calibrated and drift very slowly and the uncertainty due to finite integration time. An analytical formula to compare the theoretical $\sigma_{V_{r,i}}$ to the measured one can be derived

$$\sigma_{V_{r,i}} = \frac{1}{\sqrt{\sqrt{2}B\tau_{\text{eff}}}} \sqrt{T_A + T_{R_1}} \sqrt{T_A + T_{R_2}} \quad (18)$$

where $T_A$ refers to the physical temperature of the matched loads $T_A = T_{ph} = 290$ K, $T_{R1} = 120$ K and $T_{R2} = 90$ K are the receivers' noise temperatures, $B \approx 30$ MHz is the receivers' noise bandwidth, which is obtained by fitting the fringe-wash function by a gaussian function, $\tau_{\text{eff}}$ is the effective integration time which is related to the integration time for 1B/2L digital correlators by [*Hagen and Farley*, 1973]

$$\tau_{\text{eff}} = \frac{\tau}{2.46} \quad (19)$$

and the $\sqrt{2}$ factor in equation (18) comes from the gaussian filter model. This factor is 1 if the rectangular filter model is used [*Bará et al.*, 1996]; [*Camps*, 1996]. With these paramcters, equation (18) reduces to

$$\sigma_{V_{r,i}} = \frac{0.095 \text{ K}}{\sqrt{\tau}} \quad (20)$$

or equivalently, for the normalized correlation

$$\sigma_{\mu_{r,i}} = \frac{2.4\,10^{-4}}{\sqrt{\tau}} \quad (21)$$

Figures 7a and 7b show the radiometric sensitivity of the normalized visibility in the real and the imaginary channels ($\mu_r$, $\mu_i$), which are in good agreement with the predicted values (equation (21)). The slightly smaller error in the imaginary channel of the normalized visibility is due to the $g_i$ gain factor.

## 4. Generation of a Brightness Temperature Image by Means of Aperture Synthesis

As stated in equation (1), the generation of a brightness temperature image by means of aperture synthesis requires a set of visibility samples to be measured for different baselines, $(u,v)$ points. Following the technique described by [*Laursen and Skou*, 1994] and [*Peichl and Süß*, 1994], these baselines are measured sequentially, which implicitly assumes that the scene and the antenna temperature do not change during the measurement.

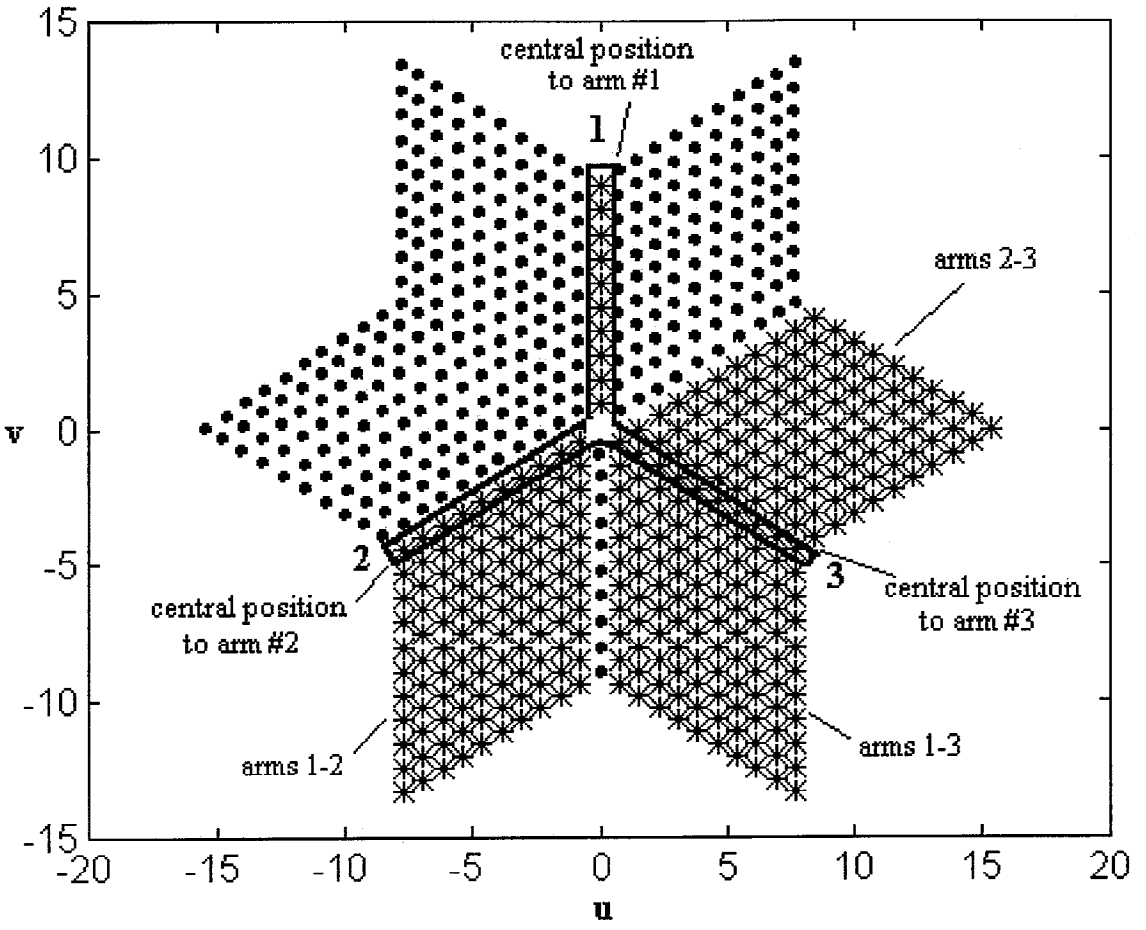


**Figure 8.** (asterisks) Measured *(u,v)* samples and (dots) *(u,v)* samples obtained by hermiticity for 10 antennas per arm spaced $d=0.89\lambda$.

### 4.1. Measurement sequence

Figure 8 shows the *(u,v)* points (asterisks) that are measured and the *(u,v)* samples obtained by the hermiticity of the visibility function (dots) for an Y array of 10 antenna positions per arm ($N_{EL}$ = 10) spaced $d$ = 0.89 wavelengths. For each antenna position, at least two measurements are made, the first one for phase tracking (see section 4.2) and the second one to measure the apparent brightness temperature distribution.

### 4.2. Tracking of phase drifts and visibility samples denormalization

Although offset and inphase errors are initially calibrated, small phase drifts have been found to have a critical impact on image recovery. Those phase drifts are mainly attributed to the phase variation introduced by the movement of the so-called phase-stable cables connecting the antennae to the mainframe. Phase variations are tracked by means of a so-called "hot point." It consists of a matched load connected to an amplifier that is connected to a pyramidal horn located right in front of the center of the Y array as shown in Plate 2. At each baseline a measurement with the "hot point" ON is performed: the phase of the visibility sample is extracted, and it is taken into account in the next measurement.

Here it must be pointed out that a hot point is expressly forbidden in the protected bands. In a full array, with all the antennas, phase variations are expected to be much smaller, due only to system drifts and not to the movement of the cables as in our two-antenna prototype. Consequently, it is expected that

full arrays will not require phase tracking at each measurement. However, some kind of periodic phase calibration procedure must be allocated (e.g. noise injection [*Torres et al.*, 1996] and the redundant space calibration [*National Radio Astronomy Observatory (NRAO)*, 1989] ).

Amplitude mismatches and quadrature errors are then calibrated according to equation (13), and visibility samples are denormalized by multiplying by the channel gain factors

$$V^{(1)} = g_1 g_2 \mu^{(1)}$$

$$g_1 = \sqrt{T_A + T_{R_1}} \; ; \quad T_{R_1} = 120 \text{ K} \tag{22}$$

$$g_2 = \sqrt{T_A + T_{R_2}} \; ; \quad T_{R_2} = 90 \text{ K}$$

The zero baseline is set as

$$V(0,0) = T_A \tag{23}$$

### 4.3. Inversion of the set of visibility samples

Since fringe-washing effects are completely negligible ($B/f_o$=0.3%), there is only a pair of antennae, and they are highly decoupled, more than 30 dB for the shortest baseline, visibility samples can be inverted by an hexagonal inverse Fourier transform and antenna pattern compensation [*Camps et al.*, 1995, 1997c]

$$T_B(\xi,\eta) = \frac{F_H^{-1}\{ W^{\text{Bl.}}(u,v)\; V^{(1)}(u,v) \}}{F_{n_1}(\xi,\eta)\; F_{n_2}{}^*(\xi,\eta)} \tag{24}$$

where $W^{\text{Bl.}}(u,v)$ is the Blackmann window with rotational symmetry and is extended up to the maximum $(u,v)$ coverage: $\rho_{MAX} = \sqrt{3}\, N_{EL}\, d$. The Blackmann window is selected because of its low secondary lobes and good radiometric accuracy. At this point it should be noted that since this inversion scheme is based on an hexagonal inverse Fourier transform, it does not require interpolations, avoids induced artifacts, and preserves signal-to-noise ratio and radiometric sensitivity, which is only degraded by the compensation of the antenna patterns.

### 4.4. Experimental results

Experimental results demonstrate the passive two-dimensional aperture synthesis concept with natural and artificial scenes:

1. The first scene consists of a measurement inside an anechoic chamber to evaluate, as far as possible, the error analysis budget performed by *Camps et al.* [1997b] and *Torres et al.* [1996].

2. The second and the third measurements are natural scenes consisting of the clearance between two buildings and the contour defined by a mountain and the sky.

3. Following the technique used by *Laursen and Skou* [1994], the fourth scene is a composition of four measurements of metallic forms over a 45° inclined plane of microwave absorbers reflecting the sky radiation. Metallic forms are made with adhesive aluminum paper glued to shaped cardboards.

**4.4.1. Measurement inside the anechoic chamber: Image error generation.** When the interferometer is put inside an anechoic chamber, microwave absorbers act as a blackbody: the antenna temperature is equal to the physical temperature of the absorbers and the apparent brightness temperature is constant in all directions. Consequently, all the visibilities should be zero, except for the zero baseline that equals the antenna temperature. However, the instrumental errors and residual calibration errors lead to a nonconstant apparent brightness temperature. The radiometric error budget in the alias free field of view is summarized in Table 1. According to *Camps et al.*, [1997b] and *Torres et al.*, [1997] the predicted radiometric accuracy is 1.46 K rms, while the standard deviation computed from the reconstructed image shown in Plate 1 is 1.73 K, with peak errors $\Delta T_{max}$= 4.1 K and $\Delta T_{min}$= - 4.9 K. This value agrees within 20% with the predicted one. Note that this budget does not include antenna pattern errors, since they are enclosed by a blackbody, nor antenna coupling effects [*Camps et al.*, 1997b]. Aliasing effects in the reconstructed image (Plate 1b) are not apparent because the average value $V(0,0) = T_A$ has been subtracted prior to the inversion of the visibility samples. The larger errors that are appreciated in the next measurements are expected to come from the variation of the brightness temperature scene being imaged during the measurement, from 90 to 120 min.

**4.4.2. Natural scene 1: Two buildings of the UPC campus seen from the street.** In the next examples, three pictures are shown for each measurement: in Plate 2 in the top left side (Plate 2a) there is a picture of the scene being imaged; in the top right side (Plate 2b) there is the alias-free field of view (FOV) reconstructed image at X band; and in the bottom right side (Plate 2c), there is the complete

**Table 1.** Radiometric Accuracy Budget: Antennas Inside an Anechoic Chamber

| Error source | Radiometric rms error, K | Comments |
|---|---|---|
| Discretization error | 0.19 | $N_{EL}$=10; $T_o$=290K |
| Finite integration time | 0.61 | NEL=10; $\tau$=2 s, Blackmann window |
| Amplitude error | 1.00 | 2% residual eccentricity (Figure 4) |
| Phase error | 0.83 | 2° residual phase error |
| Inplane antenna position error | 0.18 | 1 mm |
| Predicted radiometric accuracy | 1.46 | |

Antenna pattern errors do not need to be accounted for: antenna coupling errors can be neglected ($|S_{12}|$<-30dB at d=0.89 $\lambda$). $T_{A1}$=$T_{A2}$= physical temperature.

aliased synthetic image. It should be noted that the angular resolution for the Y array configuration with 10 antenna positions per arm, spaced 0.89 $\lambda$, and Blackmann windowing is about 4.7°, while the alias-free field of view is 34.6° wide and 42.5° height. It means that images are smooth and are composed only by 7.3 x 9.0 pixels.

Plate 2 shows UPC Campus Nord buildings C5 and D5 seen from the street. In Plate 2a the pyramidal horn antenna used as a hot point for phase tracking during the measurement is appreciated. In the synthetic image the brightness apparent temperature contour of the buildings can be appreciated over the cold brightness temperature of the sky (Plates 2b and 2c). From left to right a decreasing line due to the perspective of the buildings on the left is marked as 1, a flat zone in the middle with a peak at the position of the lamppost is marked as 2, and a vertical line for the building in the right is marked as 3.

**4.4.3. Natural scene 2: Water tank over a mountain.** Plate 3 shows a water tank over the mountain located in the right side of the picture. In Plates 3b and 3c the recovered alias-free FOV and the complete synthetic images corresponding to the previous picture can be observed. It should be noted that this image has been obtained with the Y array with five antenna positions per arm and the spatial resolution is poorer than before $\Delta\theta^{syn}_{-3\ dB}$ = 9.35°.

In Plate 3b the ground-sky border can be easily appreciated. From left to right a descent due to the brick building is marked as 1, an ascent due to the mountain, a hot spot in the center probably due to the building, is marked as 2, another ascent due to the mountain, a flat summit with a small peak due to the water tank, is marked as 3 in the region aliased with the sky, Plate 3c, and finally, another ascent due to the mountain. It is clear from Plate 3c that this is an example in which the alias-free FOV, which is in principle limited by the hexagonal periodic repetition of the unit circle [*Camps et al.*, 1997c], can be extended by substraction of the brightness offset introduced by one of the overlapping regions, in this case the sky.

**4.4.4. Metallic UPC logo and acronym over microwave absorbers.** The bottom of Plate 4 shows the logotype of the Polytechnic University of Catalonia and its acronym "UPC" formed with metallic pieces. In the top there are represented four recovered brightness temperatures images formed in four independent measurements. The three circles in the lowest side of the UPC logotype were designed to be just the size of the spot of the half-power synthesized beam width. The upper circles are of the same size, but as they are more distant, the subtended angle is smaller, and they are resolved worse. Note the shape of the microwave absorber that is outstanding over the sky in the top of the recovered image.

As in the previous images, the metallic letters "U," "P," and "C" appear at a low brightness temperature $T_{letters} \approx T_{sky}$ over a hot brightness temperature $T_{absorber} \approx T_{physical}$. The border between the apparent brightness temperature of the microwave absorber and that of the sky can be clearly observed.

## 5. Conclusions

This paper has described the hardware configuration of the UPC synthetic aperture interferometric radiometer prototype, paying special attention to its

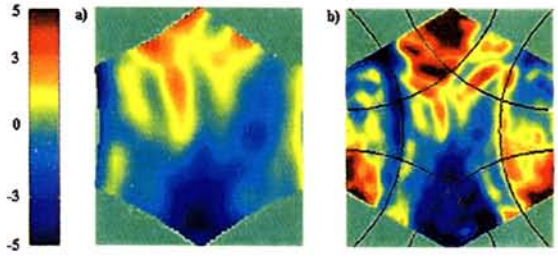


**Plate 1.** Error image measured inside an anechoic chamber $T_0$=290 K. (a) Alias-free FOV. (b) Aliased image ( $\Delta\theta_{-3\,dB} = 4.7°$).

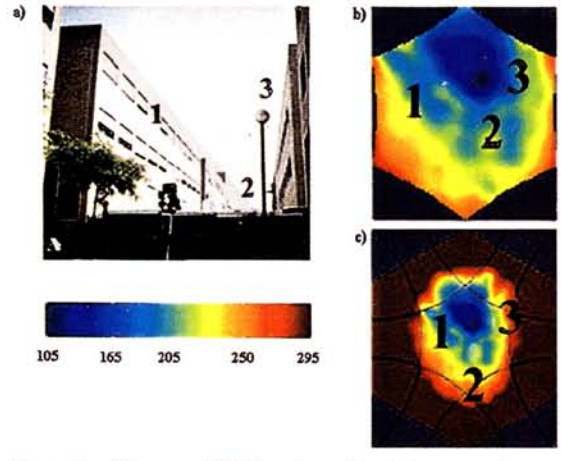


**Plate 2.** Measured X-band synthetic image of two buildings at the Campus Nord of the UPC. (a) Picture of the scene. (b) Alias-free FOV. (c) Aliased image ( $\Delta\theta_{-3\,dB} = 4.7°$).

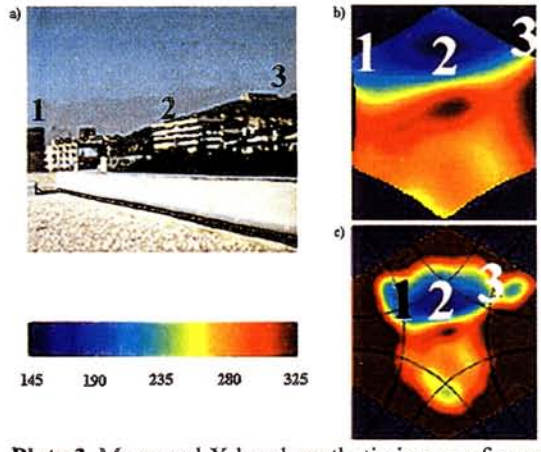


**Plate 3.** Measured X-band synthetic image of a water tank on a mountain. (a) Picture of the scene. (b) Alias free FOV. (c) Aliased image ( $\Delta\theta_{-3\,dB} = 9.4°$).

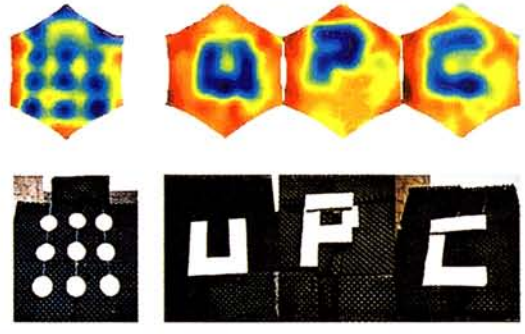

**Plate 4.** Measured X-band synthetic image of the UPC logo and its acronym made with metal strips over microwave absorbers ( $\Delta\theta_{-3\,dB} = 4.7°$).

experimental characterization and calibration. Some measured synthetic brightness temperature images have been also presented.

The main contributions of this paper are to point out the key hardware requirements and the proposal of an experimental procedure to calibrate overall receivers' and correlators' amplitude, inphase, and quadrature errors by means of the so-called "calibration circles."

**Acknowledgments.** This work has been supported by the Spanish Ministry of Education and Culture CICYT TIC 96/0879. The authors want to thank to A. Cano and J. Giner for their wotk at the workshop and the microwave laboratory.

## References

Bará, J., A. Camps, I. Corbella, and F. Torres, Bi-dimensional discrete formulation for aperture synthesis radiometers, 9777/92/NL/PB, final report, Eur. Space Agency, ESTEC, Noordwijk, Netherlands, 1996.

Camps, A., Application of Interferometric Radiometry to Earth Observation, Ph.D. thesis, Universitat Politècnica de Catalunya, Barcelona, Spain, Nov. 1996.

Camps, A., J. Bará, I. Corbella, and F. Torres, Visibility inversion algorithms over hexagonal sampling grids, in *Soil Moisture and Ocean Salinity Measurements and Radiometer Techniques, Rep. ESA WPP-87,* pp. 109-113, Eur. Space Res. and Technol. Cent., Noordwijk, the Netherlands, April 20-22, 1995.

Camps, A., F. Torres, I. Corbella, J. Barà, and J.A. Lluch,

"Threshold and Timing Errors of 1 bit/2 level digital correlators in Earth Observation Synthetic Aperture Radiometry", *Electronics Letters*, *33* (9) 812-814, 1997a.

Camps, A., J. Bará, F. Torres, I. Corbella, and J. Romeu, Impact of antenna errors on the radiometric accuracy of large aperture synthesis radiometers, *Radio Sci., 32* (2), 657-668, 1997b.

Camps, A., J. Bará, I. Corbella, and F. Torres, The processing of hexagonally sampled signals with standard rectangular techniques: Application to aperture synthesis interferometric radiometers, *IEEE Trans. Geosci. Remote Sens., 35* (1), pp. 183-190, 1997c.

Hagen, J.B., and D. Farley, Digital correlation techniques in radio science, *Radio Sci., 8*, 775-784, 1973.

Laursen, B., and N. Skou, A spaceborne synthetic aperture radiometer simulated by the TUD demonstration model, in *Proceedings of the Int. Geosci. and Remote Sens. Symp. (IGARSS 94),* pp. 1314-1316, Calif. Inst. of Technol., Pasadena, Aug. 8-12, 1994.

National Radio Astronomy Observatory (NRAO), A collection of Lectures from the Third NRAO Synthesis Imaging Summer School, vol. 6, Astron. Soc. of the Pacific, San Francisco, California, 1989.

M. Peichl, H. Süβ, Theory and design of an experimental aperture synthesis radiometer, in *Proceedings of the Progress In Electromagnetic Research Symposium PIERS 94*, Noordwijk, the Netherlands, 1994.

Ruf, C.S., C.T. Swift, A.B. Tanner, and D.M. Le Vine, Interferometric synthesis aperture microwave radiometry for remote sensing of the Earth, *IEEE Trans. Geosci. Remote Sens., 26(5)*, 597-611, 1988.

Thompson, A.R., J.M. Moran, G.W. and Swenson, *Interferometry and Synthesis in Radio Astronomy*, chap. 3 and 6, John Wiley, New York, 1986.

Torres, F., A. Camps, J. Bará, I. Corbella, and R. Ferrero, On-board phase and modulus calibration of large aperture synthesis radiometers. Study applied to MIRAS, *IEEE Trans. Geosci. Remote Sens., 34(4)*, 1000-1009, 1996.

J. Bará, A. Camps, I. Corbella, X. Soler, and F. Torres, Department of Signal Theory and Communications, Universitat Politècnica de Catalunya, Campus Nord D3-D4, c/Gran Capità s/n 08034 Barcelona, Spain. (e-mail: bara@voltor.upc.es; camps@voltor.upc.es; corbella@voltor.upc.es; torres@voltor.upc.es)

(Received December 26, 1996; revised April 14, 1997; accepted April 30, 1997.)